

## Electrical source of surface plasmon polaritons based on hybrid Au–GaAs QW structures

Cite this: *Nanoscale*, 2013, 5, 8494

Jing Li,<sup>ab</sup> Hong Wei,<sup>a</sup> Hao Shen,<sup>a</sup> Zhuoxian Wang,<sup>a</sup> Zhensheng Zhao,<sup>b</sup>  
Xuanming Duan<sup>b</sup> and Hongxing Xu<sup>\*ac</sup>

Received 27th May 2013

Accepted 26th June 2013

DOI: 10.1039/c3nr02749j

[www.rsc.org/nanoscale](http://www.rsc.org/nanoscale)

In this paper, the electrical excitation of surface plasmon polaritons (SPPs) based on a hybrid metal–semiconductor quantum well (QW) structure is investigated by finite-difference time-domain (FDTD) simulations and experiments. The metal–QW hybrid structure is made of a metal grating structure deposited on a semiconductor QW with small separation between them. When electron–hole pairs are excited using current injection into the QW, SPPs are generated and coupled out by a metal grating. The spectral and imaging measurements were performed to confirm the electrical excitation of SPPs. The hybrid structure could serve as a plasmonic source for integrated plasmonic circuits.

### Introduction

Surface plasmon polaritons (SPPs), which are electromagnetic modes confined along metal–dielectric interfaces, have attracted much interest in many application fields, especially integrated plasmonic circuits. Plasmonic circuitry is thought of as a promising candidate for future information technology because it can be much faster than its electronic counterpart and break the diffraction-limited size of the photonic circuitry.<sup>1–6</sup> Combining plasmonic structures with conventional optoelectronic integrated devices provides a possible avenue for the realization of integrated plasmonic circuits. Passive functional SPP components, such as waveguides, have been integrated with traditional photonic devices.<sup>7,8</sup> Active plasmonic devices provide the excitation,<sup>9–14</sup> amplification<sup>15–18</sup> and detection<sup>19–21</sup> of SPPs, which could pave the way for integrated plasmonic circuits.

Because of the momentum mismatch between photons and SPPs, specific schemes for momentum matching are needed to couple the light from an independent light source to the SPPs.<sup>22</sup>

The bulky light sources cannot be scaled down to the nanoscale to be integrated into plasmonic circuits. Therefore, an electrical SPP source compatible with the nanoscale plasmonic components is highly desired for the development of integrated plasmonic circuits. There have been many studies concerning the electrical excitation of surface plasmons. A metal–insulator–metal (MIM) junction structure has been demonstrated to emit light based on inelastic electron tunneling.<sup>23</sup> Recently, many systems have been investigated for the electrical excitation of SPPs based on the electrical generation of excitons, such as organic LEDs,<sup>24</sup> silicon nanocrystals,<sup>25</sup> semiconductor QW LEDs,<sup>26,27</sup> semiconductor nanowire LEDs<sup>28,29</sup> and semiconductor quantum cascade devices.<sup>30,31</sup> Despite the rapid progress in the electrical excitation of SPPs, some challenges hinder the practical applications. For example, organic emitting materials and mid-infrared quantum cascade materials are difficult to apply to integrated circuits because of the low melting temperature and long working wavelength, respectively. An alternative method is to develop the electrical SPP source using a metal structure hybrid with high gain semiconductor QW materials to generate SPPs.

In this paper, we investigated the electrical excitation of SPPs based on a metal–semiconductor QW hybrid structure. Different from the generation of SPPs solely due to the electroluminescence of LEDs coupling with the metal waveguide through a nanogap,<sup>26,27</sup> the metal–QW hybrid structure is designed to benefit the excitation of SPPs. The Au–GaAs QW hybrid structure consists of the GaAs QW and Au grating on the Au electrode deposited on the QW structure. By electrical injection into the QW, electron–hole pairs are generated in the QW and coupled into SPP modes at the metal–semiconductor interface. The generated SPPs are coupled out by the grating structure and detected through the photon emission. Besides the SPPs excited at the metal–semiconductor interface, the scattering at the edge of the grating area can generate SPPs at the metal–air interface. The emission images for the device with the coupling grating demonstrate the electrical excitation of SPPs, which is confirmed by FDTD simulations.

<sup>a</sup>Beijing National Laboratory for Condensed Matter Physics and Institute of Physics, Chinese Academy of Sciences, Beijing 100190, China. E-mail: [hxxu@iphy.ac.cn](mailto:hxxu@iphy.ac.cn)

<sup>b</sup>Lab of Organic NanoPhotonics and Key Lab of Functional Crystals and Laser Technology, Technical Institute of Physics and Chemistry, Chinese Academy of Sciences, Beijing 100190, China

<sup>c</sup>Center for Nanoscience and Nanotechnology, and School of Physics and Technology, Wuhan University, Wuhan 430072, China

## Device design

The schematic diagram of the device is shown in Fig. 1a. In the metal–semiconductor hybrid structure, the Au grating is deposited on top of the GaAs QW heterostructure. When a forward bias is applied, the electron–hole pairs in the semiconductor QW structure are electrically excited. SPPs are generated because the excited electron–hole pairs decay by direct coupling to the metal–semiconductor interface,<sup>32</sup> where the metal layer supports SPPs in a wide frequency range. The most important characteristic of the device is that it is compact, which is beneficial to integration applications.

As is well known for the interaction between dipoles and metal films, the decay rates of the dipoles vary drastically with the distance from the metal–semiconductor interface. For the excitation of SPPs generated based on the metal–QW coupling, the coupling strength is also distance dependent. The excitation efficiency of the SPPs will increase when dipoles approach the metal surface from far away. However, as the dipole is very close to the metal surface, Ohmic losses will eventually begin to prevail, which weakens the excitation of SPPs. In addition, the decay rate is related to the thickness of the metal layer since there is different coupling between SPP modes at the GaAs–Au interface and ones at the Au–air interface for metal layers with different thicknesses; the SPP mode density is also different for metal layers with different thicknesses, which affects the decay rates of the dipoles. So, it is necessary to investigate the optimum structure parameters, for example, the distance between the metal layer and the QW layer and the thickness of the metal layer.

We performed electrodynamic simulations using commercial FDTD software (Lumerical Solution) to study the decay rates of emitters for the Au–GaAs QW coupling structure. The 2D simulation model with Au grating deposited on the GaAs substrate is depicted in Fig. 2a. For the simulation, the structure is irradiated by 100 dipole sources (interval of 24 nm) with a polarization orientation difference of  $3.6^\circ$  for adjacent dipoles at a wavelength of 750 nm,<sup>26,27</sup> which are denoted by the black

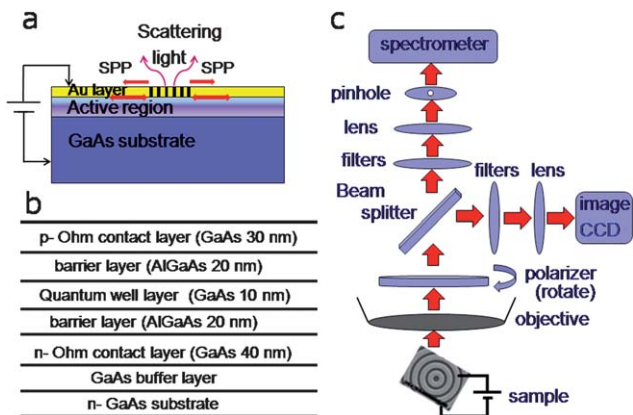


**Fig. 1** (a) Schematic diagram of the device. (b) The components of the semiconductor material. (c) Schematic of measurement setup based on a Raman spectrometer.

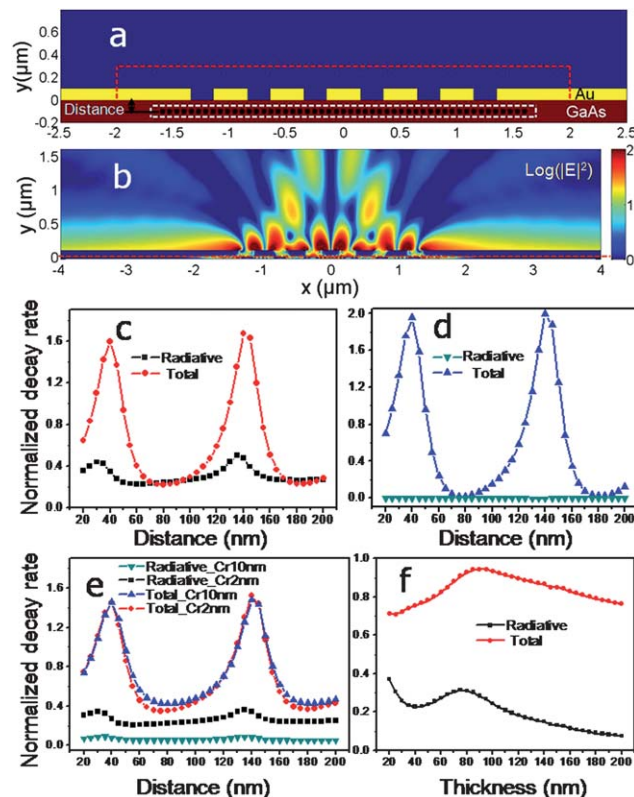


**Fig. 2** (a) The model for 2D FDTD simulation. The black dots denote the excited 100 dipole sources with a polarization orientation difference of  $3.6^\circ$  for adjacent dipoles. The white dashed line indicates the power monitor for the total decay of dipoles, while the red dashed line indicates that for the radiative decay. (b) The electric field intensity (logarithmic scale) at a free space wavelength of 750 nm (the red dashed line indicates the metal–semiconductor interface). (c–e) Normalized decay rates for radiative decay and total decay as a function of the distance of the dipole from the Au–GaAs interface for the Au–grating–GaAs structure (c), Au–film–GaAs structure (d) and Au–Cr–grating–GaAs structure (e). The thickness of the Au layer is fixed to be 100 nm in (c–e). The thickness of the Cr layer in (e) is 2 nm (black and red) and 10 nm (green and blue), respectively. (f) Normalized decay rates for radiative decay and total decay as a function of the thickness of the Au layer for the Au–grating–GaAs structure and the distance of the dipole from the Au–GaAs interface is fixed to be 50 nm. All data are normalized to the decay rates for dipoles in bulk GaAs without Au.

dots in Fig. 2a. Because the classical electromagnetic power is related to the quantum mechanical decay rate,<sup>33</sup> power monitors are used to detect the radiative decay and the total decay of the dipoles, as represented by red and white dashed lines in Fig. 2a, respectively. The period and duty cycle of the Au grating are fixed to 500 nm and 0.4, respectively. At a wavelength of 750 nm, the refractive indexes of Au and Cr are  $0.1398 + 4.532i$  and  $4.024 + 4.353i$ , respectively, according to the experimentally measured data from Johnson and Christy,<sup>34</sup> the index of GaAs is 3.7. Fig. 2b shows the electric field intensity distribution when the distance between the Au layer and the dipoles and the thickness of the Au layer are 50 nm and 100 nm, respectively. It can be found that SPPs are generated at the metal–air interface due to scattering at the Au film edge next to the grating. The generated SPPs propagate along the Au film and Au strips with a propagation length at the Au–air interface longer than that at

the Au–GaAs interface due to the high refractive index of the GaAs layer. Besides propagating SPPs, there may be a few local plasmon modes at the grating region.<sup>35,36</sup>

Fig. 2c shows the decay rates normalized to that for dipoles in bulk GaAs as a function of the distance between the dipoles and the Au–GaAs interface. When the dipoles are very close to the interface, the quenching effects are very strong which decreases the radiation intensity. As the distance increases, the total decay rates and radiative decay rates increase. The radiation peaks appear at a distance of 30 nm for radiative decay and 40 nm for total decay. When the distance is bigger than 40 nm, the decay rates decrease and then increase again. The total decay rates reach peaks at the distance of 140 nm and 243 nm (not shown). The period is about 102 nm, which is about half the light wavelength of about 202 nm in GaAs. The multi-peaks phenomenon perhaps results from the interference of the light emitted by the dipole sources and the reflected light from the metal layer.

For a 100 nm thick Au film deposited on a GaAs substrate without a grating structure, the decay rates are normalized to the ones for dipoles in bulk GaAs as a function of the distance from the Au–GaAs interface, as shown in Fig. 2d. The radiative decay rate remains at nearly zero, which suggests the light outcoupling from the SPPs could be ignored and the dipole decay channels only include Ohmic losses and generation of SPPs. Under this situation, the variation of the total decay rate with distance is similar to that shown in Fig. 2c, and also shows two peaks of the decay rate at a distance of 40 nm and 140 nm.

Fig. 2e shows the normalized decay rates as a function of the distance from the metal–semiconductor interface for the grating made of Au (100 nm thick) and Cr (2 nm or 10 nm thick) deposited on the GaAs structure. A Cr layer is usually used in experiments to increase the adhesion of the Au layer and semiconductor. It is found that the variation tendency of the total decay rates in Fig. 2e is similar to those shown in Fig. 2c and d. However, with the increase of Cr layer thickness from 2 nm to 10 nm, the intensity of the radiative decay rate is decreased sharply, which suggests a negative effect of the Cr layer for the generation of SPPs and their outcoupling into light. In fact, the 2 nm thick Cr layer is enough to increase the Au layer adhesion, and doesn't strongly decrease the radiative decay rate.

Normalized decay rates as a function of the thickness of the Au layer are presented in Fig. 2f. The decay rates change significantly with the variation of Au layer thickness, especially when the thickness is small. For a thin Au layer on a semiconductor substrate, the SPP mode density near the QW layer is large and the coupling of the SPP modes and electron–hole pairs is enhanced. However, for a thick Au layer, the total decay rates vary gently because of the little variation of the SPP mode density near the QW layer. The decay rate peaks for radiative decay and total decay are reached when the thickness of the Au layer is near 80–100 nm. According to the simulation results, the distance between the QW and Au is set to be 50 nm and the thickness of the Cr–Au layer is chosen to be 2/100 nm for the experimental device.

## Experiments

The semiconductor QW material was grown by Metal–Organic Chemical Vapor Deposition (MOCVD) on an n-type GaAs substrate according to the device design above. As shown in Fig. 1b, a 10 nm-thick GaAs QW layer was sandwiched by two 20 nm-thick  $\text{Al}_{0.35}\text{Ga}_{0.65}\text{As}$  barrier layers, with a 30 nm-thick p-Ohm GaAs layer (doping level of about  $10^{18}$ ) on the top and a 40 nm-thick n-Ohm GaAs layer (doping level of about  $10^{18}$ ) on the bottom. A tensile-strained GaAs QW was introduced in order to enhance the TM modal gains because of the transverse magnetic polarization properties of SPPs.

For possible device integration applications, the grating coupling method is attractive because the grating structure can be easily fabricated on the metal film supporting the SPPs. Here different grating structures were used for the device, and the grating period was 300–600 nm with a duty cycle of 0.4–0.5. Patterns were created on a PMMA film with a thickness of 260 nm by e-beam lithography (EBL, Raith 150), and metal structures were obtained by e-beam evaporation deposition and a lift-off process. The thickness of the Cr–Au metal structure deposition on the GaAs QW was 2/100 nm. The side of the n-type GaAs substrate was covered by Cr–Au (2/70 nm thickness), used as n-type electrode layer.

The spectra and images were acquired using a Renishaw inVia microRaman spectroscopy system. The schematic illustration of the measurement setup is shown in Fig. 1c. The current was injected by a metal probe connected to the p-type electrode, which was bigger than  $50\ \mu\text{m} \times 100\ \mu\text{m}$ . In the measurement, the optical signal was collected by a  $50\times$  long working distance objective (N.A. = 0.5) and the polarization was selected by the polarizer. All the measurements were finished at room temperature.

## Results and discussion

Fig. 3a shows the typical spectra of the device measured at the grating area with a different forward bias applied and the SEM image of the grating structure. The intensity of the spectra increases as the injection current increases. The emission bands of the device are determined by the special epitaxial material structure. Under the QW region, there is an n-type Ohm layer with a high doping level, which provides a complex recombination channel for electron–hole pairs. As shown in Fig. 3b, the maximum intensities at wavelengths of 750 nm and 878 nm vary nearly linearly with the injection current. The current–voltage curve is also plotted in Fig. 3b, where the linear variation is indicative of the current injection characteristics. Because the device was fabricated on a large semiconductor substrate, the injection current spread so that a large injection current is needed. In order to decrease the injection current, the semiconductor active region was dry etched to small regions after optical lithography and inductively coupled plasma reactive ion etching (ICP–RIE, Oxford, PlasmaLab 100) processes with an etching depth of 1  $\mu\text{m}$ . When the device is fabricated on the small semiconductor QW region of  $150\ \mu\text{m} \times 100\ \mu\text{m}$ , the injection current is reduced to 1/10. As shown in Fig. 4a, there is

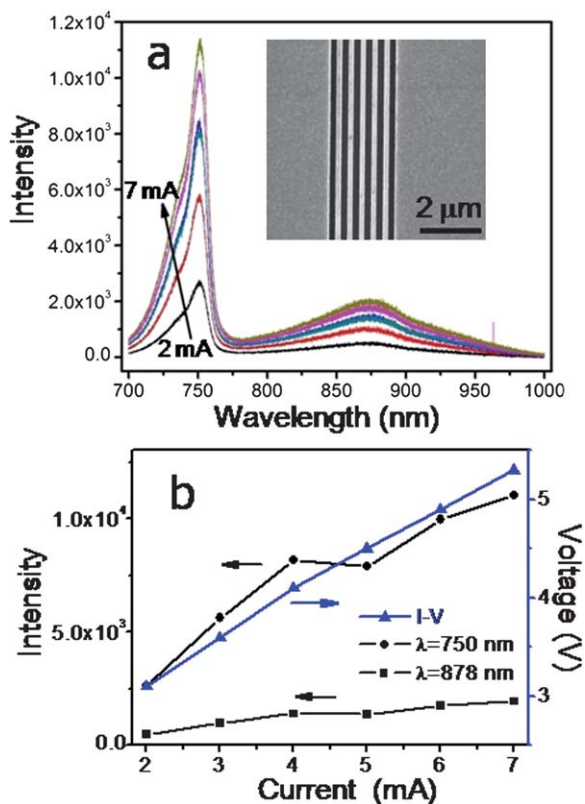


**Fig. 3** (a) The spectra measured at the grating region with integration time of 60 s at different injection currents. (The inset is the SEM image of the metal grating structure on top of the QW.) (b) Plot of the emission intensity at wavelengths of 750 nm and 878 nm as functions of injection current. The current-voltage curve is also plotted (blue curve).

an etching region (active layers etched), bare epitaxial region, Au stripe, Au grating and Au electrode from left to right.

The polarization characteristics of the device demonstrate the generation of SPPs. With an injection current of 0.5 mA for the device shown in Fig. 4a, the images of emission at a wavelength of 755 nm are recorded at different polarizations. For the image obtained with no polarizer in Fig. 4b, the intensities at both the grating region and the bare epitaxial region are strong. Fig. 4c and d show the images for the emission polarization parallel and perpendicular to the grating strips. At the grating region, the intensity with perpendicular polarization is much stronger than that with parallel polarization. For the bare epitaxial region, the intensity for different polarizations is almost the same. The intensity of the grating region is stronger than the bare epitaxial region for the perpendicular polarization, while the result is the opposite for the parallel polarization. The polarization characteristics indicate the great difference between electrically generated SPPs and non-plasmonic photon radiation.

To understand the polarization properties of the device, 2D FDTD simulation with a model according to our experiment is performed, as shown in Fig. 4e. For the irradiation dipole source with a polarization orientation perpendicular and parallel to the grating axis, the electric field distributions are

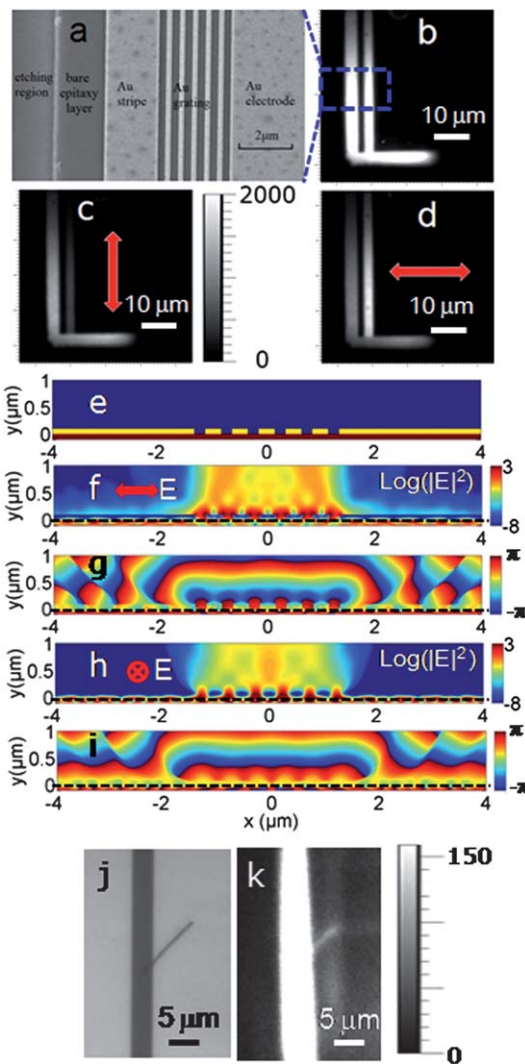


**Fig. 4** (a) SEM image of the metal structure on the etched semiconductor substrate. (b–d) Optical images for the device at a wavelength of 750 nm with an injection current of 0.7 mA and integration time of 60 s. There is a polarizer in the collecting light path and the red arrows indicate the polarization direction in (c) and (d), while there is no polarizer in (b). (e) The model of Au grating on the GaAs substrate for 2D FDTD simulation with a 100 nm-thick Au grating layer and the distance between the dipole and Au–GaAs interface of 50 nm. (f and g) The electric field intensity (logarithmic scale) and corresponding phase distribution with polarization perpendicular to the grating axis. (h and i) The results for polarization parallel to the grating axis. The black dashed lines indicate the metal–semiconductor interface in (f–i). (j) Bright field optical image for an Ag nanowire on the metal structure. (k) Optical image of the device for an emission wavelength of 750 nm with an integration time of 20 s at an injection current of 0.7 mA.

shown in Fig. 4f and h, respectively, and the corresponding phase distributions are shown in Fig. 4g and i, respectively. It is clear that SPPs are excited near the grating region and propagate along the Au waveguide for the polarization orientation perpendicular to the grating axis, however, light only passes through the grating slits for the polarization orientation parallel to the grating axis. The phase distribution near the grating region and Au–air interface, which indicates the change of electric field direction, confirms the generation and propagation of SPPs.

As the SPPs propagating along the metal–air interface cannot be directly detected in the far field, a local scatterer can be put on the metal surface to convert SPPs to photons.<sup>37,38</sup> As shown in Fig. 4j, chemically synthesized Ag nanowire is used as the scatterer. An Ag nanowire, with length 13  $\mu\text{m}$  and diameter 200 nm, was placed on the Au film close to the grating by using a micromanipulator (MMO-202ND, Narishige).<sup>39,40</sup> The whole nanowire is lit, as shown in Fig. 4k. Although one end of the nanowire is placed on the grating, the light emission along the wire is not due to the excitation of SPPs on the nanowire through the end on the grating. It is known that the SPPs on the nanowire can only be coupled out as photons at the discontinuous points on the wire, for instance the other end of the wire. Therefore, the light emission on the nanowire is not from the nanowire SPPs. Here the wire functions as a scatterer to convert the SPPs on the gold film into photons.

Besides 1D slit grating, a 2D ring grating structure was also investigated. Fig. 5a shows the Au ring grating fabricated by the same process as that for slit grating. The image at a wavelength of 755 nm was obtained for an injection current of 0.5 mA. As shown in Fig. 5b, SPPs can be coupled out from the ring grating region and the whole grating region is bright when no polarizer is added. However, under *x*- or *y*-polarization, there are only two lobe regions along the polarization direction, as shown in Fig. 5c and d. The emission patterns of different polarizations can be explained by grating-enabled SPP–photon conversion. Through 3D FDTD simulation with a model according to our experiment, the calculation agrees with the measured results. Fig. 5e shows the electric field distribution, with bright emission at the whole grating region when an unpolarized source irradiates the structure. However, as shown in Fig. 5f, there are only two bright lobe regions when the polarization is orientated parallel to the *x*-axis, which is in accordance with the measured results. The phase distribution shown in Fig. 5g demonstrates exactly the change of the electric field orientation at different lobes in Fig. 5f.

For the ring grating–QW coupling device, the time-resolved photoluminescence decay traces were measured using a pulsed laser with a wavelength of 532 nm as the pump source. A decay trace for the bare semiconductor region was also measured as a reference. As shown in Fig. 5h, the decay of the semiconductor–metal grating structure region is faster than the decay of the reference region, and the lifetime decreases from 1.7 ns to 1.3 ns. The decrease of the lifetime is due to the Purcell effect<sup>41,42</sup> resulting from the coupling between the semiconductor QW and the metal grating.

This device can be integrated with other plasmonic structures on a chip. By a bonding process, the semiconductor QW epitaxial layer on the substrate may be added to any designed place on another new substrate and then the original semiconductor substrate could be etched, which could be used to obtain a complex integrated plasmonic system. This method based on an additive process has been used in photonic devices<sup>43</sup> and we are trying to fabricate an integrated complex plasmonic structure on a Si substrate by the bonding process method.

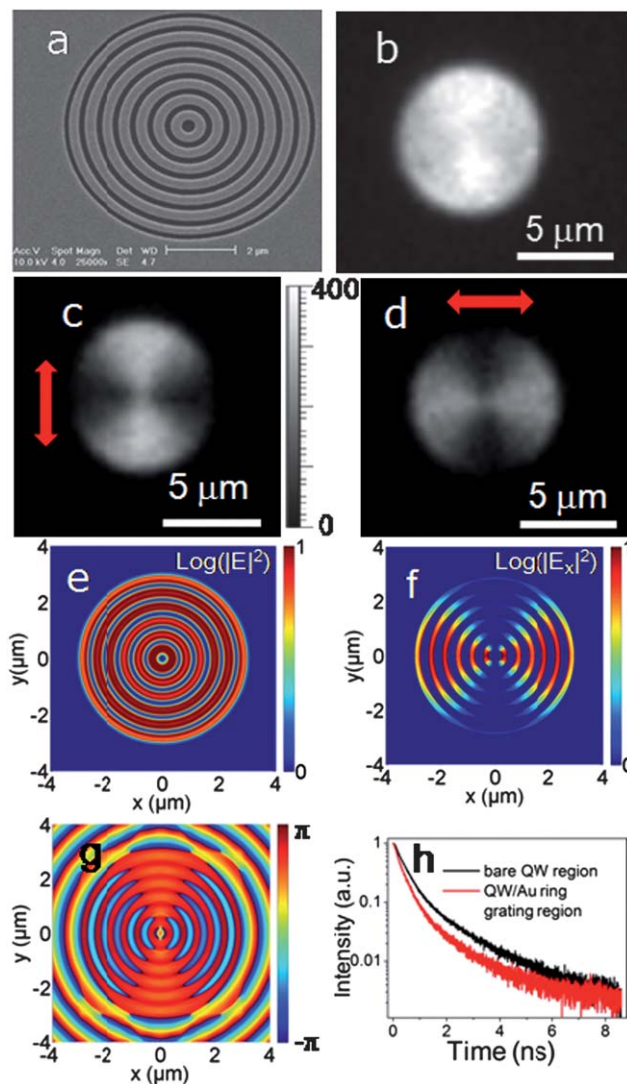


**Fig. 5** (a) SEM image of the metal ring grating structure on a GaAs QW substrate. (b–d) Optical images for the device at a wavelength of 750 nm with the integration time of 40 s. Two orthogonal polarizations shown by the red arrows are selected in (c) and (d). The intensity scale bar in (c) applies to (b) and (d) as well. (e) The electric field intensity (logarithmic scale) according to the 3D FDTD simulation with an unpolarized source. (f and g) The electric field intensity (logarithmic scale) and the phase distribution of  $E_x$  for the dipole sources polarized parallel to the *x*-axis. (h) Normalized fluorescence decays for bare QW (black curve) and the QW–Au ring grating region (red curve).

## Conclusion

In conclusion, we have realized the electrical excitation of surface plasmon polaritons based on a metal–semiconductor QW hybrid structure. The excitation of SPPs is based on the coupling of the metal layer and semiconductor QW heterostructure. When QW is excited by current injection, SPPs are generated directly and then coupled out by the slit or ring grating structures. The polarization characteristics of the emitted light confirm the electrical generation of SPPs. The electrically excited SPP source may play an important role in the development of integrated plasmonic circuits, and may

also bring new ideas for the realization of electrical plasmonic amplifiers and modulators.

## Acknowledgements

The authors acknowledge valuable discussions with Professor Peter Nordlander, Professor Naomi J. Halas, Professor Zhaowei Liu and Dr Nathaniel K. Grady. This work was supported by a MOST Grant (no. 2009CB930700), NSFC Grants (nos 11004237, 11134013, 11227407) and “Knowledge Innovation Project” (KJXC2-EW-W04) of CAS, Opened Fund of the State Key Laboratory on Integrated Optoelectronics (IOSKL2012KF10).

## Notes and references

- 1 E. Ozbay, *Science*, 2006, **311**, 189–193.
- 2 T. W. Ebbesen, C. Genet and S. I. Bozhevolnyi, *Phys. Today*, 2008, **61**, 44–50.
- 3 D. K. Gramotnev and S. I. Bozhevolnyi, *Nat. Photonics*, 2010, **4**, 83–91.
- 4 H. Wei and H. X. Xu, *Nanophotonics*, 2012, **1**, 155–169.
- 5 N. P. Leon, M. D. Lukin and H. K. Park, *IEEE J. Sel. Top. Quantum Electron.*, 2012, **18**, 1781–1791.
- 6 V. J. Sorger, R. F. Oulton, R.-M. Ma and X. Zhang, *MRS Bull.*, 2012, **37**, 728–738.
- 7 S. I. Bozhevolnyi, V. S. Volkov, E. Devaux, J. Y. Laluet and T. W. Ebbesen, *Nature*, 2006, **440**, 508–511.
- 8 S. A. Bozhevolnyi, *Plasmonic nanoguides and circuits*, Pan Stanford, Singapore, 2009.
- 9 D. J. Bergman and M. I. Stockman, *Phys. Rev. Lett.*, 2003, **90**, 027402.
- 10 M. A. Noginov, G. Zhu, A. M. Belgrave, R. Bakker, V. M. Shalaev, E. Narimanov, S. Stout, E. Herz, T. Suteewong and U. Wiesner, *Nature*, 2009, **460**, 1110–1114.
- 11 R. F. Oulton, V. J. Sorger, T. Zentgraf, R.-M. Ma, C. Gladden, L. Dai, G. Bartal and X. Zhang, *Nature*, 2009, **461**, 629–632.
- 12 M. T. Hill, M. Marell, E. S. Leong, B. Smalbrugge, Y. Zhu, M. Sun, P. J. van Veldhoven, E. J. Geluk, F. Karouta, Y. S. Oei, R. Nötzel, C. Z. Ning and M. K. Smit, *Opt. Express*, 2009, **17**, 11107–11112.
- 13 H.-S. Kwon, J.-H. Kang, C. Seassal, S.-K. Kim, P. Regreny, Y.-H. Lee, C. M. Lieber and H.-G. Park, *Nano Lett.*, 2010, **10**, 3679–3683.
- 14 Y.-J. Lu, J. Kim, H.-Y. Chen, C. H. Wu, N. Dabidian, C. E. Sanders, C.-Y. Wang, M.-Y. Lu, B.-H. Li, X. G. Qiu, W.-H. Chang, L.-J. Chen, G. Shvets, C.-K. Shih and S. Gwo, *Science*, 2012, **337**, 450–453.
- 15 M. C. Gather, K. Meerholz, N. Danz and K. Leosson, *Nat. Photonics*, 2010, **4**, 457–461.
- 16 I. D. Leon and P. Berini, *Nat. Photonics*, 2010, **4**, 1–6.
- 17 X.-J. Zhang, Y.-C. Li, T. Li, S.-Y. Lee, C.-G. Feng, L.-B. Wang and T. Mei, *Opt. Lett.*, 2010, **35**, 3075–3077.
- 18 D. Y. Fedyanin, A. V. Krasavin, A. V. Arsenin and A. V. Zayats, *Nano Lett.*, 2012, **12**, 2459–2463.
- 19 I. D. Vlamincck, P. V. Dorpe, L. Lagae and G. Borghs, *Nano Lett.*, 2007, **7**, 703–706.
- 20 A. L. Falk, F. H. L. Koppens, C. L. Yu, K. Kang, N. D. L. Snapp, A. V. Akimov, M.-H. Jo, M. D. Lukin and H. K. Park, *Nat. Phys.*, 2009, **5**, 475–479.
- 21 P. Neutens, P. V. Dorpe, I. D. Vlamincck, L. Lagae and G. Borghs, *Nat. Photonics*, 2009, **3**, 283–286.
- 22 S. A. Maier, *Plasmonics: fundamentals and applications*, Springer, New York, 2007.
- 23 S. L. McCarthy and J. Lambe, *Phys. Rev. Lett.*, 1976, **37**, 923–925.
- 24 D. M. Koller, A. Hohenau, H. Ditlbacher, N. Galler, F. Reil, F. R. Aussenegg, A. Leitner, E. J. W. List and J. R. Krenn, *Nat. Photonics*, 2008, **2**, 684–687.
- 25 R. J. Walters, R. V. A. van Loon, I. Brunets, J. Schmitz and A. Polman, *Nat. Mater.*, 2010, **9**, 21–25.
- 26 P. Neutens, L. Lagae, G. Borghs and P. V. Dorpe, *Nano Lett.*, 2010, **10**, 1429–1432.
- 27 L. Wang, T. Li, L. Li, W. Xia, X.-G. Xu and S.-N. Zhu, *Opt. Express*, 2012, **20**, 8710–8717.
- 28 P. Y. Fan, C. Colombo, K. C. Y. Huang, P. Krogstrup, J. Nygård, A. F. i. Morral and M. L. Brongersma, *Nano Lett.*, 2012, **12**, 4943–4947.
- 29 Y.-S. No, J.-H. Choi, H.-S. Ee, M.-S. Hwang, K.-Y. Jeong, E. K. Lee, M.-K. Seo, S.-H. Kwon and H.-G. Park, *Nano Lett.*, 2013, **13**, 772–776.
- 30 A. Bousseksou, J.-P. Tetienne, I. MoldovanDoyen, C. Sirtori, G. Beaudoin, I. Sagnes, Y. De Wilde and R. Colombelli, *Phys. Rev. Lett.*, 2010, **104**, 226806.
- 31 C. S. Kim, I. Vurgaftman, R. A. Flynn, M. Kim, J. R. Lindle, W. W. Bewley, K. Bussmann, J. R. Meyer and J. P. Long, *Opt. Express*, 2010, **18**, 10609–10615.
- 32 J. Kalkman, H. Gersen, L. Kuipers and A. Polman, *Phys. Rev. B: Condens. Matter Mater. Phys.*, 2006, **73**, 075317.
- 33 L. Novotny and B. Hecht, *Principles of nano-optics*, Cambridge, New York, 2006.
- 34 P. B. Johnson and R. W. Christy, Optical constants of the noble metals, *Phys. Rev. B: Solid State*, 1972, **6**, 4370–4379.
- 35 A. Degiron and T. W. Ebbesen, *J. Opt. A: Pure Appl. Opt.*, 2005, **7**, S90–S96.
- 36 D. F. P. Pile, T. Ogawa, D. K. Gramotnev, Y. Matsuzaki, K. C. Vernon, K. Yamaguchi, T. Okamoto, M. Haraguchi and M. Fukui, *Appl. Phys. Lett.*, 2005, **87**, 261114.
- 37 A. W. Sanders, D. A. Routenberg, B. J. Wiley, Y. Xia, E. R. Dufresne and M. A. Reed, *Nano Lett.*, 2006, **6**, 1822–1826.
- 38 M. W. Knight, N. K. Grady, R. Bardhan, F. Hao, P. Nordlander and N. J. Halas, *Nano Lett.*, 2007, **7**, 2346–2350.
- 39 H. Wei, Z. X. Wang, X. R. Tian, M. Kall and H. X. Xu, *Nat. Commun.*, 2011, **2**, 387.
- 40 H. Wei and H. X. Xu, *Nanoscale*, 2012, **4**, 7149–7154.
- 41 H. Iwase, D. Englund and J. Vuckovic, *Opt. Express*, 2008, **16**, 426–434.
- 42 Z. M. Wang and A. Neogi, *Nanoscale photonics and optoelectronics*, Springer, New York, 2010.
- 43 A. W. Fang, H. Park, O. Cohen, R. Jones, M. J. Paniccia and J. E. Bowers, *Opt. Express*, 2006, **14**, 9203–9210.